New Journal of Physics
The open access journal at the forefront of physics

Deutsche Physikalische Gesellschaft DPG IOP Institute of Physics

PAPER • OPEN ACCESS

Characterizing the Zeeman slowing force for $^{40}Ca^{19}F$ molecules

To cite this article: P Kaebert *et al* 2021 *New J. Phys.* **23** 093013

New Journal of Physics
The open access journal at the forefront of physics

Deutsche Physikalische Gesellschaft DPG
IOP Institute of Physics

Published in partnership with: Deutsche Physikalische Gesellschaft and the Institute of Physics

OPEN ACCESS

RECEIVED
26 April 2021

REVISED
6 August 2021

ACCEPTED FOR PUBLICATION
18 August 2021

PUBLISHED
8 September 2021

PAPER

Characterizing the Zeeman slowing force for $^{40}Ca^{19}F$ molecules

P Kaebert, M Stepanova, T Poll, M Petzold, S Xu*, M Siercke* and S Ospelkaus

Institut für Quantenoptik, Leibniz Universität Hannover, 30167 Hannover, Germany
* Authors to whom any correspondence should be addressed.

E-mail: s.xu@iqo.uni-hannover.de and siercke@iqo.uni-hannover.de

Keywords: cold molecules, Zeeman slower, spectroscopy

Abstract

In this paper we investigate the feasibility of Zeeman slowing calcium monofluoride molecules originating from a cryogenic buffer gas cell. We measure the $A^2\Pi_{1/2}(v=0, J=\frac{1}{2}) - X^2\Sigma_{1/2}$ $(v=0, N=1)$ hyperfine spectrum of CaF in the Paschen–Back regime and find excellent agreement with theory. We then investigate the scattering rate of the molecules in a molecular Zeeman slower by illuminating them with light from a 10 mW broad repumper and a 10 mW multi-frequency slowing laser. By comparing our results to theory we can calculate the photon scattering rate at higher powers, leading to a force profile for Zeeman slowing. We show results from a simple 1D simulation demonstrating that this force is narrow enough in velocity space to lead to significant velocity compression, and slowing of the molecules to trappable velocities.

1. Introduction

Owing to their internal degrees of freedom, molecular systems have the ability to probe fundamental physics and investigate states of matter dominated by long-range interactions. The ability to investigate these physical phenomena is directly linked to the number of molecules we can trap in experiments, as well as the temperatures to which we can cool them. To this end, experiments on laser cooling molecules have had incredible success, realizing magneto-optical traps [1–5], molasses [6–10], magnetic [11–13] and electrostatic traps [14] as well as optical traps [6, 10, 15]. Loading molecules into these traps generally requires a method of slowing a molecular beam down to velocities on the order of 10 m s^{-1}. Currently, the most efficient experimentally realized method of laser slowing of molecules is chirped light slowing [16], where a fast moving molecular pulse, originating from a cryogenic buffer gas cell, is slowed down via photon scattering from a pulse of chirped light. The chirp of the laser is timed to compensate for the Doppler shift of the molecules as they are being slowed by the beam. Chirped light slowing is especially compatible with current buffer gas beam sources [17], which deliver relatively short (in time) pulses of molecules. In contrast, the predominant method of slowing down atoms using radiation pressure is the Zeeman slower [18]. Here, instead of compensating for the Doppler shift with a chirp in the laser frequency, the Doppler shift is counteracted by a corresponding Zeeman shift from a magnetic field. By choosing the correct spatial variation of this magnetic field, a Zeeman slower is able to slow atoms to rest without the need to chirp the laser frequency, and without needing to know the time the atoms enter the slowing region. Zeeman slowing, unlike chirped light slowing, is thus a continuous slowing method, and would allow for the use of continuous molecular beam sources [19]. This, coupled with the fact that the atoms are slowed down at a specific point in space, rather than a point in time, is the reason why atomic experiments opt for Zeeman slowing rather than chirped light slowing.

Zeeman slowing for molecules is not as straightforward as it is for atoms, due to the fact that molecular slowing schemes operate on a type-II transition ($J \rightarrow (J-1)$-transition). While this is necessary to achieve a quasi-closed cycling transition, it results in the molecules cycling between essentially all the ground and excited state Zeeman sublevels. Since Zeeman slowing relies on compensating the Doppler shift with a Zeeman shift, it requires all transitions the molecules undergo to have the same Zeeman shift, which is not the case for every Zeeman sublevel.

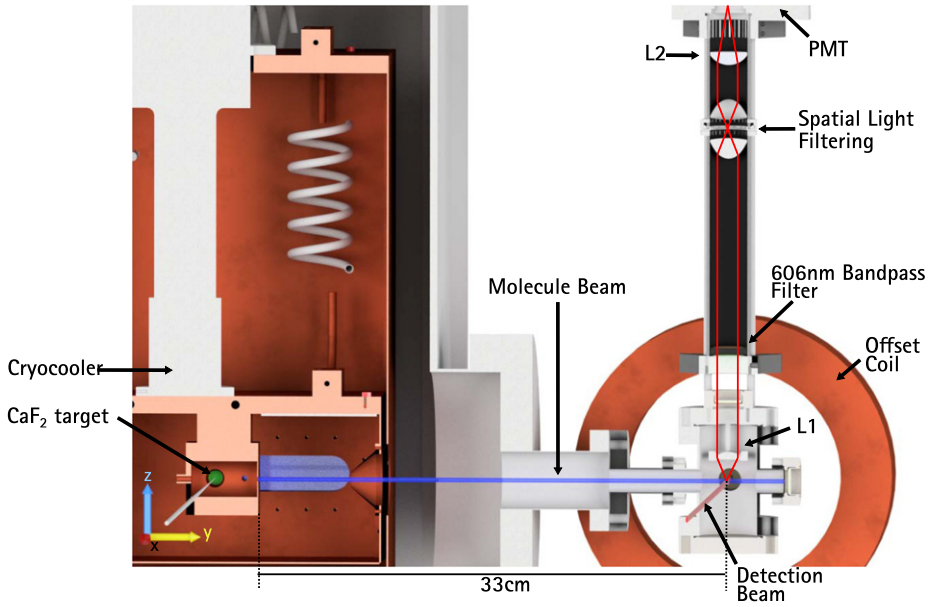

Figure 1. Setup of the experiment. Molecules are introduced into a cryogenic buffer gas cell via laser ablation of a CaF_2 target, resulting in a beam of CaF molecules exiting the cell (along y-axis). 33 cm away from the cell the CaF molecules enter the imaging region, where they are illuminated by either one or more LIF (light induced fluorescence, along x-axis) beams. A pair of coils can be used to generate a magnetic field along the imaging beam propagation direction, enabling spectroscopy of the molecules in magnetic fields up to 300 G.

Nevertheless, Zeeman slowing of molecules was proposed to be possible [20] by entering the Paschen–Back regime with a sufficiently high magnetic field. At such fields, the Zeeman shifts become highly regular, resembling a three-level system with two ground state manifolds ($m_s = \pm 1/2$) and the excited state manifold (figure 2(f)). Coupling the $m_s = +1/2$ manifold to the excited state using a multi-frequency slowing laser results in a velocity selective force, tunable by magnetic field. Molecules that are lost from the slowing cycle by falling into the $m_s = -1/2$ manifold are repumped into the slowing cycle by the addition of one frequency-broad repump laser. This type-II Zeeman slower was shown to be capable of slowing potassium atoms on the D_1−line at efficiencies close to what a regular Zeeman slower is capable of [21]. Zeeman slowing of an actual molecule however, has not yet been achieved.

In this paper, we measure the velocity dependence of the Zeeman slowing force for calcium monofluoride (CaF) molecules in magnetic fields between 200 G and 300 G. We first measure the strength and frequency of the individual hyperfine transitions of the $A^2\Pi_{1/2}(v = 0, J = \frac{1}{2}) - X^2\Sigma_{1/2}(v = 0, N = 1)$ manifold at these fields by scanning a single frequency laser through the transition region. We then investigate the Zeeman slowing force by looking at the fluorescence of our molecular beam when it is illuminated by both a broad repump laser and a multi-frequency slowing laser. Unlike the schemes in [20–22] we do not tailor our slowing laser frequencies or polarization. Instead, the slowing laser contains both σ^+ and σ^- polarizations and is frequency broadened by modulation of the laser current.

2. Setup and characterization of CaF transitions in the Paschen–Back regime

The basic setup of our experiment is shown in figure 1. Our molecular beam is generated via laser ablation of a CaF_2 target inside a cryogenic helium buffer gas cell. The beam exits the cell through a 3 mm aperture and enters the detection region 33 cm away from the exit. In the detection region, a 2.0 mm wide by 4.5 mm high elliptical beam with horizontal polarization (along y-direction) intersects the molecular beam at a 90° angle, and the resulting fluorescence is collected onto a PMT running in photon counting mode. Using this setup we resolve lines with a separation as close as (9 ± 1) MHz. A previous measurement of the A–X transition of CaF in high magnetic fields had a resolution of 35 MHz (FWHM) and thus was not capable of resolving all individual hyperfine transitions [23]. Two magnetic field coils surround the detection region, capable of producing a magnetic field of up to 300 G along the propagation direction of the detection laser (in x-direction), allowing us to drive both σ^+ and σ^- transitions with linear polarization, as was proposed in [20].

The detection laser consists of a laser diode at 995 nm, amplified by a tapered amplifier and mixed with an amplified 1550 nm commercial fiber laser in a MgO:PPLN crystal. The resulting 606 nm light is

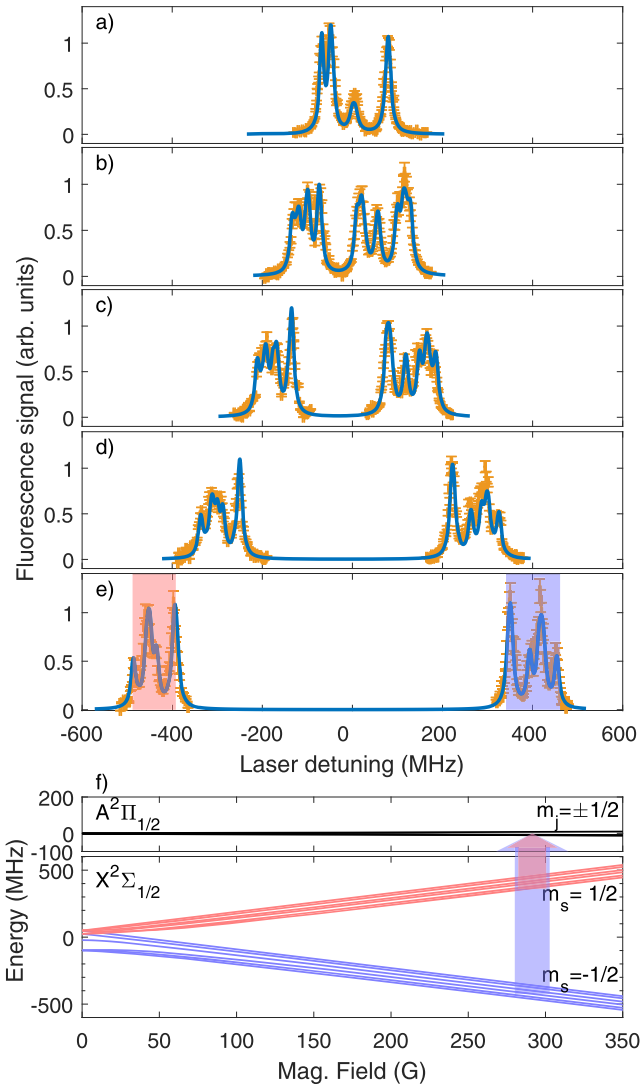

Figure 2. LIF Spectrum of CaF in fields of (a) 0 G, (b) 50 G, (c) 100 G, (d) 200 G and (e) 300 G. The orange points show the measured relative scattered photon number for a single frequency detection laser. The blue line is the result of a corresponding rate equation model with a vertical scaling factor and a horizontal shift (common in all plots) as the only free parameters. The left (red) and right (blue) rectangles in (e) and the respective arrows in the level scheme in the Paschen–Back regime indicate respectively the widths of the slowing and repumper laser used to generate the Zeeman slower force. In (f) we show the energy levels participating in Zeeman slowing along with the respective lasers addressing the slowing (red) and repumping (blue) manifolds.

stabilized on a scanning transfer cavity [24, 25] which is locked on a reference laser stabilized by a potassium spectroscopy cell. The resulting frequency stability of the 606 nm light is ≈1 MHz, measured by beating two individual 606 nm systems, locked on the same cavity, together. While this measurement does not account for any mutual drift of the two frequencies, our measurements on the molecular transitions did not show any evidence of such a drift.

Figure 2(a) shows the fluorescence signal of the molecules when no magnetic field is applied as the detection laser is scanned through the A–X resonances. The laser power used in the figure is 25 μW to avoid power broadening due to the absence of photon cycling in this measurement. Also shown in the figure is the result of a rate equation calculation (see [26]) taking into account the interaction time between the molecules and the detection laser. The transition frequencies and strengths used by the program are calculated by converting the molecular states into the Hund's case (a) basis [27] and calculating expectation values of the full Hamiltonian as well as the transition dipole matrix elements [28]. The details of this calculation are given in appendix A. Both the relative transition frequencies and the relative transition strengths measured in figure 2 are in excellent agreement with theory.

Figures 2(b)–(e) show the CaF fluorescence at magnetic fields of 50 G, 100 G, 200 G and 300 G. Again, both the relative positions and heights of the fluorescence peaks fit extremely well to theory. Figure 2(f) shows the involved levels from 0 G to the Paschen–Back regime and illustrates, which levels are addressed by which laser for the Zeeman slower force measurement (in 300 G).

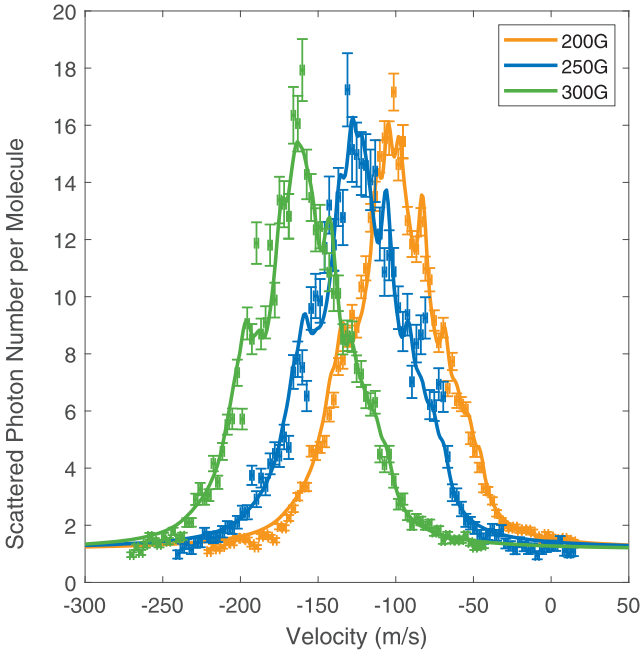

Figure 3. Scattered photon number vs slowing beam detuning of the molecules traversing the overlapped slowing and repumper beams at 200 G, 250 G and 300 G. The theory fits the data well with the molecular velocity as the only free parameter. The resulting velocity agrees reasonably well with our estimates for the beam velocity based on arrival times at the detector, giving a photon scattering rate of 3.6×10^6 s^{-1}.

2.1. Measurement of the Zeeman slowing force

Using the knowledge that our theoretical prediction of the transition strengths and relative transition frequencies is accurate, we now turn to measure the velocity dependence of the force a molecule would experience in a type-II Zeeman slower. To this end, we illuminate the molecules with both a repump laser, broadened to 120 MHz by current modulation and a multi-frequency slowing laser addressing the different hyperfine components. Instead of carefully choosing the frequencies or polarizations of the slowing laser we measure the scattering rate to compute the force when the slowing laser is frequency modulated to a width of 96 MHz. At first glance it is not obvious that such a modulation can still provide a narrow enough force profile, since strong FM modulation will inherently result in a frequency spectrum with a tail. For the Zeeman slower force, however, we limit the modulation of the slowing laser to a modulation index of 3.9, resulting in a much sharper frequency cutoff than the one traditionally seen in white light slowing. Together with a modulation frequency of 12 MHz, this gives our slowing laser its width of 96 MHz, just enough to address all the transitions in the left cluster of peaks in figure 2(e) indicated by the left (red) shaded region. The width of the broad repumper is indicated with the right (blue) shaded region. It should be noted, that in an actual Zeeman slower we would have to broaden the repumper much more, to cover all Zeeman and Doppler shifts the molecules experience, but our simulations show little dependence on the repumper width. In light of this we only modulate the repumper 'enough' to realize the Zeeman slower force, thereby avoiding excessive stray light from the apparatus due to excessive repumper power [1]. The number of photons scattered by the CaF molecules as they are illuminated by the broad repumper (10 mW) and slowing laser (10 mW) is shown in figure 3 for magnetic fields of 200 G, 250 G and 300 G. Also plotted in the figure is the result of our rate equation model. At each magnetic field the frequency of the broad repump laser is held fixed, while the slowing laser is scanned just as it was for the single frequency measurements in section 2 to simulate the force as a function of Doppler shift. As such, we plot the number of photons scattered in figure 3 as a function of velocity, rather than detuning of the laser.

As was the case with figure 2, there is excellent agreement between the rate equation simulation and the experimental data. Two important conclusions can be drawn from this agreement. Firstly, no coherent dark states are formed during the application of the slowing force. Since our model would not be able to capture these dark states, their signature would be a decrease in the photon scattering rate compared to what our model predicts. While the schemes in [20–22] attempt to circumvent these dark states via carefully

[1] This results in a repumper only slightly broader than the slowing laser. To stay in line with [20–22] however, we will maintain the distinction between 'multi-frequency' for the slower versus 'broadened' for the repumper.

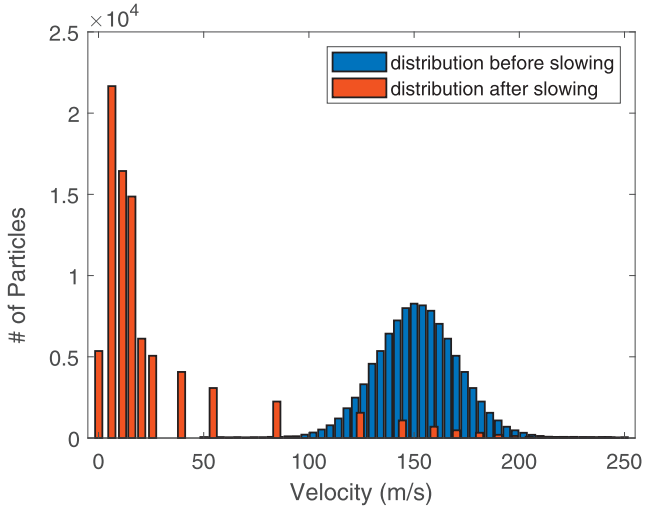

Figure 4. Simulated velocity distribution before and after Zeeman slowing. For the chosen parameters see text.

choosing the slowing frequencies or polarizations, our results demonstrate that simple frequency modulation at 12 MHz is good enough to destabilize them. Secondly the good agreement between the model and the experiment allows us to extract the photon scattering rate, and thus the magnitude of the Zeeman slowing force acting upon the molecules. To do this, we operate in a regime where, in the absence of scattering from the slowing laser, the repumper saturates the photon scattering rate. This results in the background signal in figure 3, which, due to saturation, is almost independent of the laser power and the interaction time with the molecules. Due to this independence on experimental parameters we therefore know how many photons each molecule scatters when the slowing beam is far off-resonant, which calibrates the vertical axis in figure 3. From the ratio between the on-resonant and the off-resonant photon scattering number we can then extract the interaction time of the molecules with the laser beams to be 4.4 μs. This time is consistent with our laser beam diameter and estimated buffer gas beam velocity (based on arrival time at the detector, see appendix B), and thus gives us a photon scattering rate of 3.6×10^6 s^{-1} for our parameters.

2.2. Simulating Zeeman slowing

With the data from figures 2 and 3 confirming the accuracy of our rate equation calculation, we now know the photon scattering rate as a function of Doppler shift and magnetic field, and can thus simulate if the resulting force profiles are narrow enough in velocity space and large enough in magnitude to allow for efficient Zeeman slowing. It should be noted, however, that the interaction times and powers for the measurement in figure 3 were chosen such that decay to the $v = 1$ ground state would be small. The necessity to eventually cycle molecules that have dropped to $v = 1$ back to the vibrational ground state doubles the number of states coupled to the excited state, thus reducing the slowing force by a factor of essentially two [20]. Figure 4 shows the result of a simple 1D simulation [22] of the molecular velocity before and after Zeeman slowing, taking this factor of 2 reduction in the force into account. The initial velocity distribution in the theory is centered on a velocity of 150 m s^{-1} with a width of 50 m s^{-1}. The magnetic field assumed in the simulation follows the standard square root Zeeman slower profile from 400 G to 600 G [18]. The choice of the magnetic field range 400–600G avoids any influence of the Zeeman slowing beams on magneto-optical trapping. The simulation assumes a 995 mW cm^{-2} repump laser modulated by 12 MHz to a width of 960 MHz, and a 240 mW cm^{-2} slowing laser modulated by 15 MHz to a width of 120 MHz. The center frequency of the slowing laser is chosen to slow molecules with velocities up to 180 m s^{-1}. The length of the slowing region is 0.6 m. As can be seen in the figure, the initially broad, fast molecular velocity distribution is compressed and shifted down to 15 m s^{-1} by the Zeeman slowing force, indicating that the profiles measured in figure 3 are indeed narrow enough, and provide enough photon scattering, to efficiently compress and slow the velocity distribution of the molecular beam.

3. Conclusion

We have measured the hyperfine spectrum of the $A^2\Pi_{1/2}(v = 0, J = \frac{1}{2}) - X^2\Sigma_{1/2}(v = 0, N = 1)$ transition in CaF for magnetic fields up to 300 G. We have found excellent agreement both in position and height of

the transition peaks compared to a rate equation model, with a measurement resolution of (9 ± 1) MHz. To measure the force a molecule would experience inside a type-II Zeeman slower we have measured the LIF signal of the molecules when subjected to 10 mW of light from a 120 MHz broad repumper laser and a 96 MHz broad slowing laser, addressing the six lower, and six upper ground state hyperfine levels respectively. We again found excellent agreement with theory, measuring a peak photon scattering number of 16 photons in the 4.4 μs the molecules spend inside the laser beams, demonstrating that we are already cycling between ground state sublevels at these modest interaction times and powers. We modeled 1D Zeeman slowing of CaF using the force profiles given by the rate equation model, including effects from $v = 1$ repumping, and found effective slowing and compression of molecules down to 15 m s^{-1}, where they can be captured by an MOT. Our findings directly show that efficient Zeeman slowing is possible with reasonable laser powers, and that a simple modulation of the slowing beam destabilizes any dark states while keeping the force profile narrow enough for velocity compression. With all the building blocks experimentally proven, there seem to be no obstacles on the road to realizing a Zeeman slower for molecules.

Acknowledgments

PK, M St and MS thank the DFG for financial support through RTG 1991. We gratefully acknowledge financial support through Germany's Excellence Strategy-EXC-2123/1 QuantumFrontiers.

Data availability statement

The data that support the findings of this study are available upon reasonable request from the authors.

Appendix A. Calculating the eigenenergies and transition rates of CaF

Our approach to calculating the energies and eigenstates of CaF in various magnetic fields is essentially taken from [27]. We summarize our method here for clarity as well as to highlight a discrepancy in [27]. The calculation of the transition matrix elements is based off of appendix A in [28]. For a great complementary discussion of the various parts of the Hamiltonian, see [29]. The molecular Hamiltonian for a particular electronic state can be divided up into different parts:

$$\hat{H} = \hat{H}_{\mathrm{so}} + \hat{H}_{\mathrm{ss}} + \hat{H}_{\mathrm{rot}} + \hat{H}_{\mathrm{sr}} + \hat{H}_{\mathrm{LD}} + \hat{H}_{\mathrm{F}} + \hat{H}_{\mathrm{dip}} + \hat{H}_{\mathrm{z}}. \tag{A.1}$$

Here, $\hat{H}_{\mathrm{so}}$ is the spin–orbit interaction, $\hat{H}_{\mathrm{ss}}$ is the spin–spin interaction (zero in our case), $\hat{H}_{\mathrm{rot}}$ is the rotational part, $\hat{H}_{\mathrm{sr}}$ describes the spin-rotation interaction, $\hat{H}_{\mathrm{LD}}$ the lambda doubling, $\hat{H}_{\mathrm{F}}$ and $\hat{H}_{\mathrm{dip}}$ are hyperfine terms describing the Fermi contact and magnetic dipolar interaction respectively, and $\hat{H}_{\mathrm{z}}$ describes the Zeeman interaction of the molecule. For Σ states $\hat{H}_{\mathrm{LD}} = 0$, while $\hat{H}_{\mathrm{LD}}$ takes on the role of $\hat{H}_{\mathrm{sr}}$ for Π states, and $\hat{H}_{\mathrm{sr}} = 0$. In order to write down the specific form of each of these terms in the Hamiltonian we will need to choose a basis. Unfortunately, for the case of laser-coolable molecules, the ground and excited states are best described with a different set of quantum numbers. The excited, $A\Pi_{1/2}$ State is quasi-diagonal in a Hunds case (a) basis $|\Lambda, S, \Sigma, \Omega, J, m_j, I, m_i\rangle$ while the $X\Sigma_{1/2}$ ground state is best described in Hunds case (b) $|\Lambda, N, S, J, m_j, I, m_i\rangle$. Since the choice of basis is arbitrary we choose to work in the Hunds case (a) basis. Following section 9.4.2 (c) in [27] we write the explicit form of the rotational and spin–orbit terms as

$$\begin{aligned}
&\langle \Lambda, S, \Sigma, \Omega, J, m_j, I, m_i | \hat{H}_{\mathrm{rot}} + \hat{H}_{\mathrm{so}} | \Lambda, S, \Sigma', \Omega', J, m_j, I, m_i \rangle \\
&\quad = \delta_{\Omega,\Omega'}\delta_{\Sigma,\Sigma'}[B_0\{J(J+1) + S(S+1) - 2\Omega\Sigma - \Lambda^2\} + A\Lambda\Sigma] \\
&\qquad - 2B_0 \sum_{q=\pm 1} (-1)^{J+S-\Omega-\Sigma} \begin{pmatrix} J & 1 & J \\ -\Omega & q & \Omega' \end{pmatrix} \begin{pmatrix} S & 1 & S \\ -\Sigma & q & \Sigma' \end{pmatrix} \\
&\qquad \times \sqrt{J(J+1)(2J+1)S(S+1)(2S+1)},
\end{aligned} \tag{A.2}$$

where B_0 is the rotational constant of the $v = 0$ vibrational state.

From [30] we find

$$\begin{aligned}
&\langle \Lambda, S, \Sigma, \Omega, J, m_j, I, m_i | \hat{H}_{\rm sr} | \Lambda, S, \Sigma', \Omega', J, m_j, I, m_i \rangle \\
&\quad = \delta_{\Sigma,\Sigma'} \delta_{\Omega,\Omega'} \gamma [\Omega\Sigma - S(S+1)] \\
&\qquad + \gamma \sum_{q=\pm 1} (-1)^{J+S-\Omega-\Sigma} \begin{pmatrix} J & 1 & J \\ -\Omega & q & \Omega' \end{pmatrix} \begin{pmatrix} S & 1 & S \\ -\Sigma & q & \Sigma' \end{pmatrix} \\
&\qquad \times \sqrt{J(J+1)(2J+1)S(S+1)(2S+1)},
\end{aligned} \tag{A.3}$$

with γ the spin-rotation constant.

From equation (9.66) in [27]

$$\begin{aligned}
&\langle \Lambda, S, \Sigma, \Omega, J, m_j, I, m_i | \hat{H}_{\rm LD} | \Lambda', S, \Sigma', \Omega', J, m_j, I, m_i \rangle \\
&\quad = \sum_{r=\pm 1} \delta_{\Lambda',\Lambda\pm 2} \left\{ \delta_{\Sigma,\Sigma'} \frac{q}{2\sqrt{6}} (-1)^{J-\Omega} \begin{pmatrix} J & 2 & J \\ -\Omega & -2r & \Omega' \end{pmatrix} \right. \\
&\qquad \times \sqrt{(2J-1)(2J)(2J+1)(2J+2)(2J+3)} + (p+2q)(-1)^{J+S-\Omega-\Sigma} \\
&\qquad \times \begin{pmatrix} J & 1 & J \\ -\Omega & -r & \Omega' \end{pmatrix} \begin{pmatrix} S & 1 & S \\ -\Sigma & r & \Sigma' \end{pmatrix} \\
&\qquad \left. \times \sqrt{J(J+1)(2J+1)S(S+1)(2S+1)} \right\}.
\end{aligned} \tag{A.4}$$

Here, p and q are the lambda doubling parameters of the state.

The two hyperfine terms are given in [27] in the $|\Lambda, S, \Sigma, \Omega, J, I, F, m_f\rangle$ basis in equations (9.47) and (9.49) (although there is a factor 1/2 discrepancy between 7.156 and 9.61) as

$$\begin{aligned}
&\langle \Lambda, S, \Sigma, \Omega, J, I, F, m_f | \hat{H}_{\rm F} | \Lambda, S, \Sigma', \Omega', J', I, F, m_f \rangle \\
&\quad = b_{\rm F} \sum_{q=-1}^{1} (-1)^{I+J'+F+S-\Sigma+J-\Omega} \\
&\qquad \times \sqrt{I(I+1)(2I+1)(2J+1)(2J'+1)S(S+1)(2S+1)} \\
&\qquad \times \begin{Bmatrix} J' & I & F \\ I & J & 1 \end{Bmatrix} \begin{pmatrix} J & 1 & J' \\ -\Omega & q & \Omega' \end{pmatrix} \begin{pmatrix} S & 1 & S \\ -\Sigma & q & \Sigma' \end{pmatrix},
\end{aligned} \tag{A.5}$$

and

$$\begin{aligned}
&\langle \Lambda, S, \Sigma, \Omega, J, I, F, m_f | \hat{H}_{\rm dip} | \Lambda, S, \Sigma', \Omega', J', I, F, m_f \rangle \\
&\quad = \sqrt{30} t (-1)^{I+J'+F+S+q-\Sigma+J-\Omega} \\
&\qquad \times \sqrt{I(I+1)(2I+1)(2J+1)(2J'+1)S(S+1)(2S+1)} \begin{Bmatrix} J' & I & F \\ I & J & 1 \end{Bmatrix} \\
&\qquad \times \begin{pmatrix} J & 1 & J' \\ -\Omega & q & \Omega' \end{pmatrix} \begin{pmatrix} 1 & 2 & 1 \\ q & 0 & -q \end{pmatrix} \begin{pmatrix} S & 1 & S \\ -\Sigma & q & \Sigma' \end{pmatrix}.
\end{aligned} \tag{A.6}$$

The constants $b_{\rm F}$ and t are related to the b and c parameters of Frosch and Foley [31] by $b_{\rm F} = b + 1/3c$ and $t = c/3$. To write the hyperfine terms in our uncoupled $|\Lambda, S, \Sigma, \Omega, J, m_j, I, m_i\rangle$ basis we write equation (5.79) in [27] explicitly as

$$\begin{aligned}
|\Lambda, S, \Sigma, \Omega, J, m_j, I, m_i\rangle = &\sum_{F=|J-I|}^{J+I} \sum_{m_f=-F}^{F} (-1)^{-J+I-m_f} \sqrt{2F+1} \\
&\times \begin{pmatrix} J & I & F \\ m_j & m_i & -m_f \end{pmatrix} |\Lambda, S, \Sigma', \Omega', J', I, F, m_f\rangle
\end{aligned} \tag{A.7}$$

Table A1. Molecular constants used for the $X^2\Sigma_{1/2}$ and $A^2\Pi_{1/2}$ states of CaF. Note that the values of b and c for the $A^2\Pi_{1/2}$ state are not known as of yet. The values here are chosen to give the correct 4.8 MHz hyperfine splitting.

	$X\Sigma^2_{1/2}$	$A^2\Pi_{1/2}$
A (cm^{-1})	—	72.617 43
B_0 (cm^{-1})	0.343 47	0.347 395
γ (cm^{-1})	0.001 322	—
q (cm^{-1})	—	−0.000 2916
p (cm^{-1})	—	−0.0446
b (MHz)	109.2	3.92
c (MHz)	40.1	−18.25
g_L'	1	1
g_S	2.0023	2.0023

and compute the matrix elements of $\hat{H}_{\mathrm{F}}$ and $\hat{H}_{\mathrm{dip}}$ in our uncoupled basis as sums of the matrix elements in the coupled basis.

Finally, we write the Zeeman part of the Hamiltonian as in [27] equation (9.71), neglecting the nuclear and rotational g-factors (which are ~ 1000 times smaller than the electronic ones) as

$$\begin{aligned}
&\langle \Lambda, S, \Sigma, \Omega, J, m_j, I, m_i | \hat{H}_z | \Lambda', S, \Sigma', \Omega', J, m_j, I, m_i \rangle \\
&= \mu_{\mathrm{B}} B_z \delta_{\Lambda,\Lambda'} \sum_{q=-1}^{1} (-1)^{J-m_j+J-\Omega} \sqrt{(2J+1)(2J'+1)} \begin{pmatrix} J & 1 & J' \\ -m_j & 0 & m_j \end{pmatrix} \\
&\times \begin{pmatrix} J & 1 & J' \\ -\Omega & q & \Omega' \end{pmatrix} \left\{ g_L' \Lambda \delta_{\Sigma,\Sigma'} + g_S (-1)^{S-\Sigma} \sqrt{S(S+1)(2S+1)} \right. \\
&\left. \times \begin{pmatrix} S & 1 & S \\ -\Sigma & q & \Sigma' \end{pmatrix} \right\} - \mu_{\mathrm{B}} B_Z \sum_{q=\pm 1} \delta_{\Lambda',\Lambda\pm 2} (-1)^{J-m_j} \sqrt{(2J+1)(2J'+1)} \\
&\times \begin{pmatrix} J & 1 & J' \\ -m_j & 0 & m_j \end{pmatrix} \left[(g_l' - g_r^{e'}) (-1)^{S-\Sigma} \begin{pmatrix} S & 1 & S \\ -\Sigma & q & \Sigma' \end{pmatrix} \sqrt{S(S+1)(2S+1)} \right. \\
&\times (-1)^{J-\Omega} \begin{pmatrix} J & 1 & J' \\ -\Omega & -q & \Omega' \end{pmatrix} - g_r^{e'} \delta_{\Sigma,\Sigma'} (-1)^{J-\Omega} \sum_{\Omega''} \frac{1}{2} \left\{ (-1)^{J-\Omega''} \right. \\
&\times \begin{pmatrix} J & 1 & J \\ -\Omega & -q & \Omega'' \end{pmatrix} \begin{pmatrix} J & 1 & J' \\ -\Omega'' & -q & \Omega' \end{pmatrix} \sqrt{J(J+1)(2J+1)} + (-1)^{J'-\Omega''} \\
&\left. \left. \times \begin{pmatrix} J & 1 & J' \\ -\Omega & -q & \Omega'' \end{pmatrix} \begin{pmatrix} J' & 1 & J' \\ -\Omega'' & -q & \Omega' \end{pmatrix} \sqrt{J'(J'+1)(2J'+1)} \right\} \right], \qquad \text{(A.8)}
\end{aligned}$$

where μ_{B} is the Bohr magneton, B_z an externally applied magnetic field, g_L' is the orbital g-factor and g_S is the g-factor for the electron spin. The factors g_l' and $g_r^{e'}$ can be computed from the lambda-doubling parameters to be [23] $g_l' = p/(2B_0)$ and $g_r^{e'} = -q/B_0$. Values for all the necessary parameters in the case of CaF are listed in table A1.

To calculate the eigenstates and eigenenergies at the magnetic fields of interest to us we diagonalize the Hamiltonian in (A.1). The energies vs magnetic field of the relevant ground state ($N = 1$) and excited state ($J = \frac{1}{2}$) levels are plotted in figure A1.

To find the relative strengths of the optical transitions, we calculate the transition dipole matrix elements between final and initial eigenstates $\langle f | \hat{d}_{\mathrm{p}} | i \rangle$, where p denotes the polarization of the laser. Following [28, 30] we can write the matrix elements in the uncoupled basis using the Wigner–Eckart theorem as:

$$\begin{aligned}
&\langle \Lambda, S, \Sigma, \Omega, J, m_j, I, m_i | \hat{d}_{\mathrm{p}} | \Lambda', S, \Sigma', \Omega', J', m_j', I, m_i \rangle \\
&= (-1)^{J-m_j} \begin{pmatrix} J & 1 & J' \\ -m_j & p & m_j' \end{pmatrix} \langle \Lambda, S, \Sigma, \Omega, J, I || \hat{\boldsymbol{d}} || \Lambda', S, \Sigma', \Omega', J', I \rangle. \qquad \text{(A.9)}
\end{aligned}$$

The last term on the right-hand side can be further simplified to

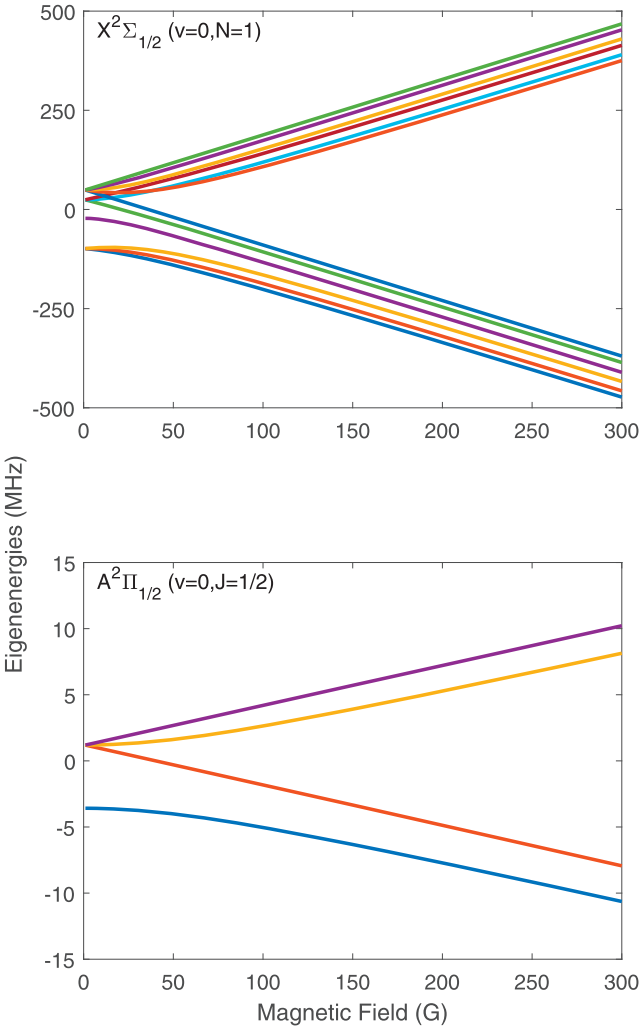

Figure A1. Eigenenergies of the $X^2\Sigma_{1/2}(v=0, N=1)$ (upper plot) and $A^2\Pi_{1/2}(v=0, J=\frac{1}{2})$ (lower plot) manifolds of CaF, found by diagonalizing the molecular Hamiltonian given in (A.1).

$$\langle \Lambda, S, \Sigma, \Omega, J, I||\hat{\boldsymbol{d}}||\Lambda', S, \Sigma', \Omega', J', I\rangle$$
$$= \sum_{q=-1}^{1} (-1)^{J-\Omega}\sqrt{(2J+1)(2J'+1)}\begin{pmatrix} J & 1 & J' \\ -\Omega & q & \Omega' \end{pmatrix}\delta_{\Sigma,\Sigma'}\langle \Lambda, S, \Sigma||\hat{\boldsymbol{d}}||\Lambda', S, \Sigma'\rangle, \tag{A.10}$$

where we have made use of the fact that the dipole operator does not couple to the spin degrees of freedom and thus $\Sigma = \Sigma'$. Since the last term in (A.10) is the same for all transitions, we can calculate the relative transition strengths between eigenstates of $\hat{H}$ without further simplification. Table A2 shows the transition strengths at high magnetic fields (Paschen–Back regime) between the states in figure A1.

Transition strengths below 0.003 are set to zero for the purpose of readability. The ground states have m_s, m_i and m_N as good quantum numbers, whereas the excited states are better described by m_j and m_i. Two important conclusions can be drawn by looking at the transition strengths: on one hand it is possible to couple every ground state level to the excited states using only σ^+ and σ^- light. On the other hand, in some instances two ground state levels need to be coupled to the same excited state, which may lead to the formation of coherent dark states. The fact that only σ^+ and σ^- light are needed, allows us to build a longitudinal Zeeman slower, where slowing light travels along the magnetic field direction. In the experiment, when modulating the slowing laser at 12 MHz to a width of 96 MHz we see no evidence of coherent dark states lowering the radiation pressure force.

Appendix B. Extracting the interaction time

To extract a value for the scattering rate of the molecules, and thus the force exerted on them, one needs to know the interaction time between the molecules and the laser beam as well as the number of photons

Table A2. Transition strengths between the $A^2\Pi_{1/2}(v=0, J=\frac{1}{2})$ and $X^2\Sigma_{1/2}(v=0, N=1)$ states of $^{40}Ca^{19}F$ at a magnetic field of 1000 G. Strengths under 0.003 are set to zero for visual clarity. Transitions driven by σ^--polarized light are colored blue, those driven by π-polarized light are colored brown, and σ^+ transition are denoted in red. Note that the normalization convention (sum of all decays from each upper level is 1) is slightly broken due to rounding errors.

$X^2\Sigma_{1/2}$	$A^2\Pi_{1/2}$			
	$m_j=\frac{1}{2}, m_i=\frac{1}{2}$	$m_j=\frac{1}{2}, m_i=-\frac{1}{2}$	$m_j=-\frac{1}{2}, m_i=-\frac{1}{2}$	$m_j=-\frac{1}{2}, m_i=\frac{1}{2}$
$m_s=-\frac{1}{2}, m_i=\frac{1}{2}, m_N=1$	0.33	0	0	0.17
$m_s=-\frac{1}{2}, m_i=\frac{1}{2}, m_N=0$	0.34	0	0	0
$m_s=-\frac{1}{2}, m_i=\frac{1}{2}, m_N=-1$	0	0	0	0.17
$m_s=-\frac{1}{2}, m_i=-\frac{1}{2}, m_N=1$	0	0.33	0.17	0
$m_s=-\frac{1}{2}, m_i=-\frac{1}{2}, m_N=0$	0	0.34	0	0
$m_s=-\frac{1}{2}, m_i=-\frac{1}{2}, m_N=-1$	0	0	0.17	0
$m_s=\frac{1}{2}, m_i=-\frac{1}{2}, m_N=-1$	0	0.16	0.33	0
$m_s=\frac{1}{2}, m_i=-\frac{1}{2}, m_N=0$	0	0	0.33	0
$m_s=\frac{1}{2}, m_i=-\frac{1}{2}, m_N=1$	0	0.17	0	0
$m_s=\frac{1}{2}, m_i=\frac{1}{2}, m_N=-1$	0.16	0	0	0.33
$m_s=\frac{1}{2}, m_i=\frac{1}{2}, m_N=0$	0	0	0	0.33
$m_s=\frac{1}{2}, m_i=\frac{1}{2}, m_N=1$	0.17	0	0	0

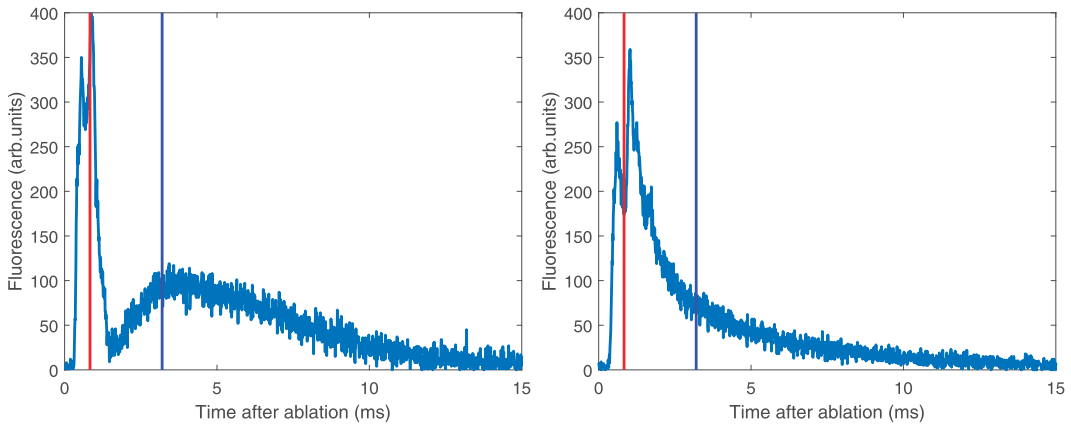

Figure B1. Time traces of the molecular signal show the resilience of the initial fast shockwave. On the left there is an additional signal of slower molecules, which was not stable over time. On the right we measure mostly a shockwave with a decaying tail. The data in this experiment was taken with this type of signal. The vertical lines indicate the expected arrival times of molecules in the detection region assuming a molecular velocity of 450 m s^{-1} (red) and 150 m s^{-1} (blue). These arrival times include our estimate for the time the molecules spend inside the buffer gas cell of 1 ms [32] for the blue line and 100 μs for the red line.

scattered in this time. We calibrate the number of photons scattered by (see main text) measuring the fluorescence signal in a regime where we saturate the photon scattering number to a known value. The interaction time on the other hand can be extracted from the laser beam diameter as well as the forward velocity of the molecular beam. The expected forward velocity of a single stage cryogenic buffer gas cell is usually close to 150 m s^{-1}, but it should be noted, that the forward velocity of our molecular beam was significantly higher than this value for the data depicted in this paper. Due to our simplified vacuum setup (see figure 1) there was no vacuum pump attached to the detection region, resulting in a high pressure attenuating the molecular beam. In figure B1 we compare the timetraces of two kinds of signals. On the left we show a combination of a fast shockwave with some slow molecules, which was rare and not stable over time due to the high background pressure. The prevailing case for our shown measurements is represented by the timetrace on the right, which exhibits high stability and mostly a shockwave with a decaying tail.

By observing the arrival times at the detector, we directly see, that the velocity of our molecules is closer to 450 m s^{-1} rather than 150 m s^{-1}.

To corroborate this result, we look at the hyperfine spectrum of the molecules as a function of laser power when a single laser frequency detection laser is used. The resolution of the hyperfine lines depends on the interaction time with the laser, because after a few scattered photons the molecules will fall into a ground state that is far off resonant with the laser beam. As such, the more time the molecule spends inside the laser beam, the less power is needed to scatter the maximum number of photons, optically pumping it out of the bright state. More power or a longer interaction time would thus result in the broadening of the spectral lines.

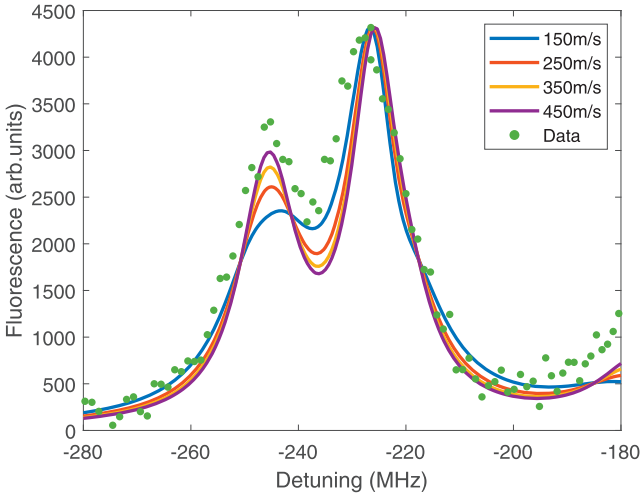

(a) 25 µW

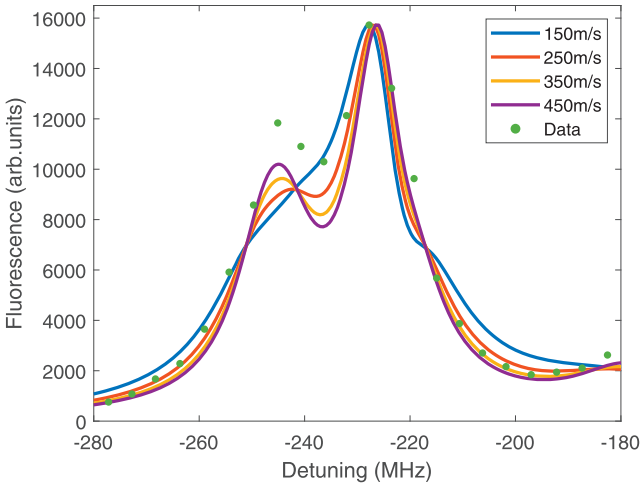

(b) 50 µW

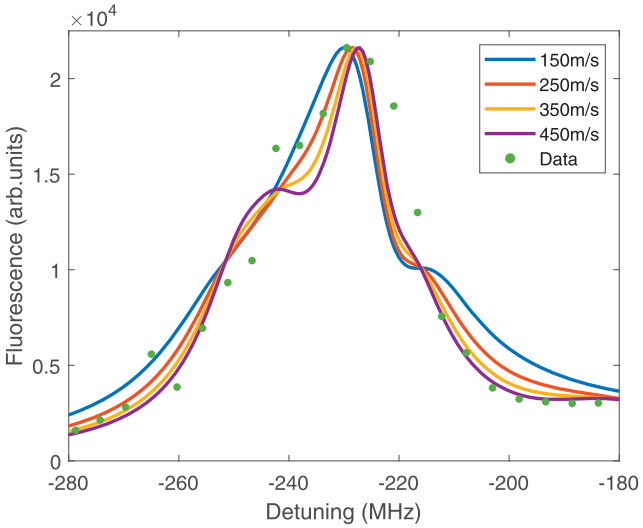

(c) 100 µW

Figure B2. Measured fluorescence signals when exciting the two $J = 3/2$ ($F = 1$ and $F = 2$) ground states with a laser power of 25 μW (a), 50 μW (b) and 100 μW (c). The solid lines are our rate equation simulations assuming various molecular beam velocities. A velocity of 450 m s^{-1} shows much better agreement with the data than a velocity of 150 m s^{-1}.

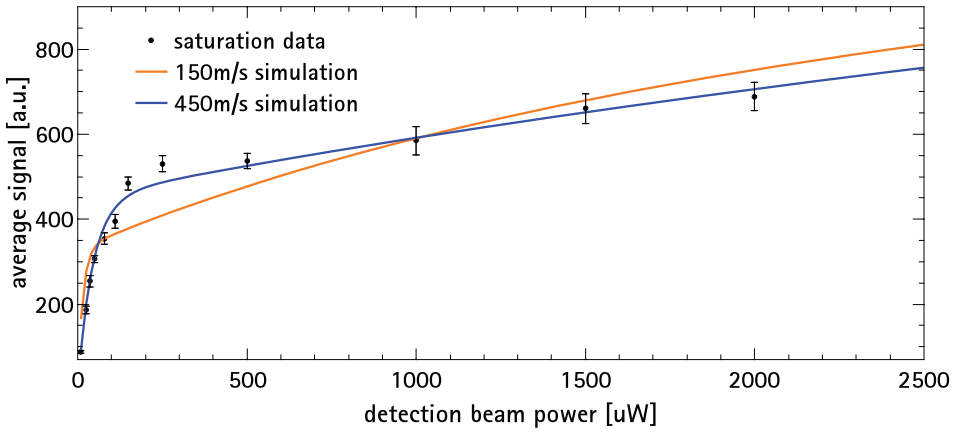

(a) Single peak LIF signal in 200 G for varying power. Simulation for 150 m/s and 450 m/s

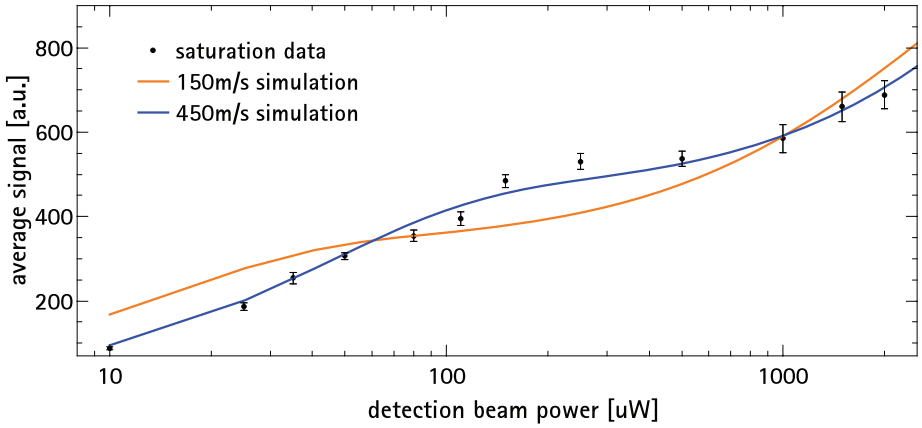

(b) Single peak LIF signal in 200 G for varying power. Simulation for 150 m/s and 450 m/s. Logarithmic power scale to demonstrate the fit over wide range.

Figure B3. Saturation behaviour of CaF used to determine molecular velocity.

We used our rate equation simulation to calculate the number of scattered photons for a single frequency detection laser with the well known transition strengths in 0 G. Comparing these results with measurements of the hyperfine spectrum for different laser powers thus gives an estimate of the forward velocity of the molecular beam. Slower (higher) velocities would saturate at lower (higher) powers, leading to a loss in resolution at lower (higher) laser power. In figures B2(a)–(c) we show the fluorescence signal on the $X^2\Sigma_{1/2}(v=0, N=1, J=\frac{3}{2}, F=1)$ and $X^2\Sigma_{1/2}(v=0, N=1, J=\frac{3}{2}, F=2)$ to the $A^2\Pi_{1/2}(v=0, J=\frac{1}{2})$ transitions. Additionally we show the corresponding sets of simulations results. The points for these measurements are not normalized to account for the decay of the ablation target, but nevertheless the figures show that a velocity of 450 m s^{-1} best reproduces our frequency resolution as a function of power.

We also confirmed this experimentally in a magnetic field. We used a 200 G offset field and measured the saturation for single prominent peak of the 'slowing manifold' (see figure 2(d)), peak at −250 MHz). We observed the number of scattered photons versus detection beam power and compared this to a simulation for this detuning in 200 G and for varying power, taking the modified transition strengths in a high magnetic field into account (see figures B3(a) and (b)). We find a strong agreement over several orders of magnitude with our observation, when we consider the forward velocity to be 450 m s^{-1} rather than 150 m s^{-1}.

We definitely observe molecules faster than 'usual' and the simulation for 0 G gives us a consistent lower bound for the velocity of 450 m s^{-1}. This bound on the velocity and our beam parameters lead to the upper bound for the interaction time of 4.4 μs. The interaction time is also consistent with our observed saturation in high magnetic fields.

Separately, as mentioned in the main text, we find the same value for the case with two modulated lasers in high magnetic field (see figure 3). There, we compared the background of the signal (where only the repumper scatters photons on resonance and optically pumps into the uncoupled slowing manifold) with the peak (where the combination of repumper and slowing laser leads to cycling). We are therefore confident in our estimation of interaction time and forward velocity of the molecules. While the molecules entering our detection region have a velocity distribution rather than a single velocity, all our measurements show that modeling them with a single, average velocity of 450 m s^{-1} is sufficient to reproduce all of our results.

ORCID iDs

P Kaebert https://orcid.org/0000-0003-1099-8495
M Siercke https://orcid.org/0000-0002-1514-8038

References

[1] Barry J F, McCarron D J, Norrgard E B, Steinecker M H and DeMille D 2014 Magneto-optical trapping of a diatomic molecule *Nature* **512** 286–9
[2] Williams H J, Truppe S, Hambach M, Caldwell L, Fitch N J, Hinds E A, Sauer B E and Tarbutt M R 2017 Characteristics of a magneto-optical trap of molecules *New J. Phys.* **19** 113035
[3] Collopy A L, Ding S, Wu Y, Finneran I A, Anderegg L, Augenbraun B L, Doyle J M and Ye J 2018 3D magneto-optical trap of yttrium monoxide *Phys. Rev. Lett.* **121** 213201
[4] McCarron D J, Norrgard E B, Steinecker M H and DeMille D 2015 Improved magneto-optical trapping of a diatomic molecule *New J. Phys.* **17** 035014
[5] Norrgard E B, McCarron D J, Steinecker M H, Tarbutt M R and DeMille D 2016 Submillikelvin dipolar molecules in a radio-frequency magneto-optical trap *Phys. Rev. Lett.* **116** 063004
[6] Anderegg L, Augenbraun B L, Bao Y, Burchesky S, Cheuk L W, Ketterle W and Doyle J M 2018 Laser cooling of optically trapped molecules *Nat. Phys.* **14** 890–3
[7] Truppe S, Williams H J, Hambach M, Caldwell L, Fitch N J, Hinds E A, Sauer B E and Tarbutt M R 2017 Molecules cooled below the Doppler limit *Nat. Phys.* **13** 1173–6
[8] Kozyryev I, Baum L, Matsuda K, Augenbraun B L, Anderegg L, Sedlack A P and Doyle J M 2017 Sisyphus laser cooling of a polyatomic molecule *Phys. Rev. Lett.* **118** 173201
[9] Ding S, Wu Y, Finneran I A, Burau J J and Ye J 2020 Sub-Doppler cooling and compressed trapping of YO molecules at μK temperatures *Phys. Rev.* X **10** 021049
[10] Cheuk L W, Anderegg L, Augenbraun B L, Bao Y, Burchesky S, Ketterle W, John M and Doyle J M 2018 Λ-enhanced imaging of molecules in an optical trap *Phys. Rev. Lett.* **121** 083201
[11] Caldwell L, Devlin J A, Williams H J, Fitch N J, Hinds E A, Sauer B E and Tarbutt M R 2019 Deep laser cooling and efficient magnetic compression of molecules *Phys. Rev. Lett.* **123** 033202
[12] Williams H J, Caldwell L, Fitch N J, Truppe S, Rodewald J, Hinds E A, Sauer B E and Tarbutt M R 2018 Magnetic trapping and coherent control of laser-cooled molecules *Phys. Rev. Lett.* **120** 163201
[13] McCarron D J, Steinecker M H, Zhu Y and DeMille D 2018 Magnetic trapping of an ultracold gas of polar molecules *Phys. Rev. Lett.* **121** 013202
[14] Prehn A, Ibrügger M, Glöckner R, Rempe G and Zeppenfeld M 2016 Optoelectrical cooling of polar molecules to submillikelvin temperatures *Phys. Rev. Lett.* **116** 063005
[15] Anderegg L, Cheuk L W, Bao Y, Burchesky S, Ketterle W, Ni K-K and Doyle J M 2019 An optical tweezer array of ultracold molecules *Science* **365** 1156–8
[16] Truppe S, Williams H J, Fitch N J, Hambach M, Wall T E, Hinds E A, Sauer B E and Tarbutt M R 2017 An intense, cold, velocity-controlled molecular beam by frequency-chirped laser slowing *New J. Phys.* **19** 022001
[17] Doyle J M, Friedrich B, Kim J and Patterson D 1995 Buffer-gas loading of atoms and molecules into a magnetic trap *Phys. Rev.* A **52** R2515–8
[18] Phillips W D and Metcalf H 1982 Laser deceleration of an atomic beam *Phys. Rev. Lett.* **48** 596–9
[19] Shaw J C and McCarron D J 2020 Bright, continuous beams of cold free radicals *Phys. Rev.* A **102** 041302
[20] Petzold M, Kaebert P, Gersema P, Siercke M and Ospelkaus S 2018 A Zeeman slower for diatomic molecules *New J. Phys.* **20** 042001
[21] Petzold M, Kaebert P, Gersema P, Poll T, Reinhardt N, Siercke M and Ospelkaus S 2018 Type-II Zeeman slowing: characterization and comparison to conventional radiative beam-slowing schemes *Phys. Rev.* A **98** 063408
[22] Liang Q, Bu W, Zhang Y, Chen T and Yan B 2019 Improvements on type-II Zeeman slowing of molecules through polarization selectivity *Phys. Rev.* A **100** 053402
[23] Devlin J, Tarbutt M R, Kokkin D L and Steimle T C 2015 Measurements of the Zeeman effect in the $A^2\Pi$ and $B^2\Sigma^+$ states of calcium fluoride *J. Mol. Spectrosc.* **317** 1–9
[24] Seymour-Smith N, Blythe P, Keller M and Lange W 2010 Fast scanning cavity offset lock for laser frequency drift stabilization *Rev. Sci. Instrum.* **81** 075109
[25] Subhankar S, Restelli A, Wang Y, Rolston S L and Porto J V 2019 Microcontroller based scanning transfer cavity lock for long-term laser frequency stabilization *Rev. Sci. Instrum.* **90** 043115
[26] Tarbutt M R 2015 Magneto-optical trapping forces for atoms and molecules with complex level structures *New J. Phys.* **17** 015007
[27] Brown J M and Carrington A 2003 *Rotational Spectroscopy of Diatomic Molecules* 1st edn (Cambridge: Cambridge University Press)

[28] Wall T E, Kanem J F, Hudson J J, Sauer B E, Cho D, Boshier M G, Hinds E A and Tarbutt M R 2008 Lifetime of the A ($v' = 0$) state and Franck–Condon factor of the A–X (0–0) transition of CaF measured by the saturation of laser-induced fluorescence *Phys. Rev.* A **78** 062509
[29] Fitch N J and Tarbutt M R 2021 Laser cooled molecules (arXiv:2103.00968)
[30] Asensio Ramos A and Trujillo Bueno J 2006 Theory and modeling of the Zeeman and Paschen–Back effects in molecular lines *Astrophys. J.* **636** 548–63
[31] Frosch R A and Foley H M 1952 Magnetic hyperfine structure in diatomic molecules *Phys. Rev.* **88** 1337–49
[32] Hutzler N R, Lu H-I and Doyle J M 2012 The buffer gas beam: an intense, cold, and slow source for atoms and molecules *Chem. Rev.* **112** 4803–27